In Pursuit of 2D Materials for Maximum Optical Response

Sunny Gupta, Sharmila N. Shirodkar, Alex Kutana, and Boris I. Yakobson*

Department of Materials Science and NanoEngineering, Rice University, Houston, Texas 77005, United States

S *Supporting Information*

ABSTRACT: Despite being only a few atoms thick, single-layer two-dimensional (2D) materials display strong electron−photon interactions that could be utilized in efficient light modulators on extreme subwavelength scales. In various applications involving light modulation and manipulation, materials with strong optical response at different wavelengths are required. Using qualitative analytical modeling and first-principles calculations, we determine the theoretical limit of the maximum optical response such as absorbance (*A*) and reflectance (*R*) in 2D materials and also conduct a computational survey to seek out those with best *A* and *R* in various frequency ranges, from mid-infrared to deep-ultraviolet. We find that 2D boron has broadband reflectance *R* > 99% for >100 layers, surpassing conventional thin films of bulk metals such as silver. Moreover, we identify 2D monolayer

semiconductors with maximum response, for which we obtain quantitative estimates by calculating quasiparticle energies and accounting for excitonic effects by solving the Bethe−Salpeter equation. We found several monolayer semiconductors with absorbances $\gtrsim$30% in different optical ranges, which are more than half of the maximum possible value, $A_{lim} = 1/2$, for a freestanding 2D material. Our study predicts 2D materials which can potentially be used in ultrathin reflectors and absorbers for optoelectronic application in various frequency ranges.

KEYWORDS: *2D materials, optics, GW+BSE, transfer matrix, absorbance limit, band nesting, black phosphorus, van der Waals heterostructure*
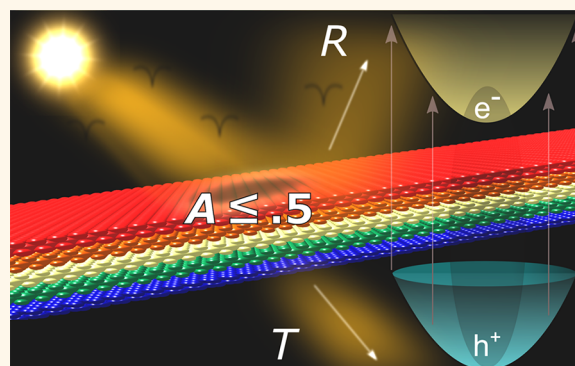
Due to their reduced dimensionality, two-dimensional (2D) materials exhibit an extraordinary optical response in comparison with bulk counterparts,[1−4] as has been shown early on with the examples of graphene and 2D MoS$_2$.[5−7] The most well-known of 2D materials, graphene, has its low-frequency absorbance defined by the universal analytical constant ($\pi/137$) $\sim$ 0.023.[1] In 2D, the joint density of states can exhibit logarithmic singularities,[8] resulting in enhanced absorption. In addition, spatial confinement and reduced dielectric screening of 2D materials causes strong Coulomb interactions that beget more stable exciton formation with large binding energy and oscillator strength compared to that of bulk crystals,[9] also enhancing their optical properties. Being a prototypical 2D semiconductor, 2D MoS$_2$ has exceptional optical absorption/photoluminescence in the visible range. Its astounding optical properties have opened up prospects for 2D material exploration for use as absorbers, reflectors, and modulators[10] in optical nanodevices such as photodiodes, solar cells, photocatalytic cells, phototransistors, and photodetectors.[11−16] These materials host stable room-temperature excitons and are ideal candidates for understanding light−matter interactions and possible application in development of excitonic polariton devices.[17]

For a variety of applications, 2D materials with strong optical response (such as absorbance and reflectance) in different frequency ranges (mid-, near-infrared (IR), visible, near-, mid-, deep-ultraviolet (UV)) are necessary, but a cohesive study estimating the transmittance, absorbance, and reflectance (*TAR*) of 2D materials is still lacking. Also, maximum achievable values of *TAR* in 2D materials have not been analyzed. For instance, it is unclear whether there are any limitations on *TAR* in 2D, for example, whether a 2D layer could be as absorbing/reflecting as a bulk material. Being at the ultimate limit of atomic size in one direction, 2D materials can also serve as elementary building blocks in more sophisticated structures such as metamaterials, where a nontrivial layer-dependent optical response emerges. It is of interest to find out atomically thin monolayers that can provide the strongest absorbance/reflectance and how close these can approach the limiting values for a 2D material.

Here, we use first-principles calculations to evaluate the *TAR* of a wide variety of 2D materials (55 monolayers), over a wide
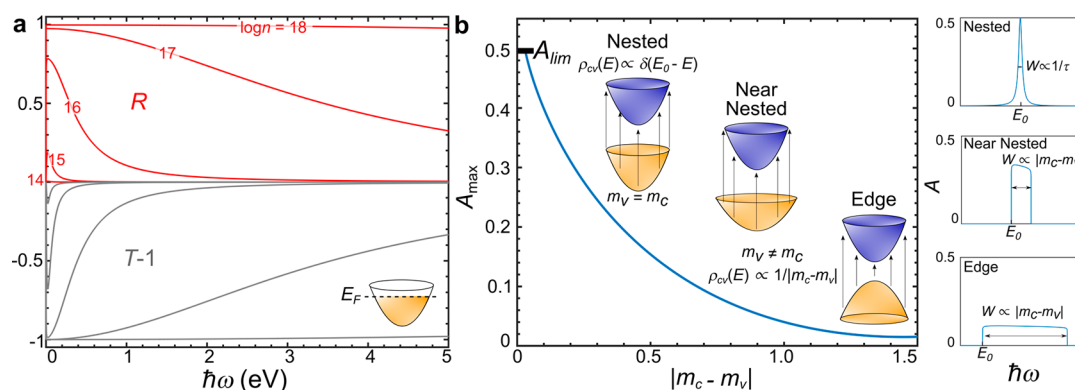
Figure 1. (a) Reflectance R and transmittance T of a model two-dimensional metal described as a 2D electron gas for electron concentrations of n between 10^{14} and 10^{18} cm^{-2}. The values for absorbance A in the visible range are small (<0.01) and not shown for clarity. Other fixed parameters are $m = m_e$, $\tau = 30$ fs, and $k_F^2 = 2\pi n$. (b) Calculated maximum absorbance of a model two-band semiconductor with different joint densities of states (ρ_{cv}) depending on the effective masses of the valence (m_v) and conduction bands (m_c) as a function of $|m_c - m_v|$. Perfect nesting, $m_c = m_v$; absorbance has a narrow peak with the width inversely proportional to scattering time τ and maximum value reaching $A_{lim} = 1/2$ (top right panel). Nearly perfect nesting, $m_c \neq m_v$ and $m_c, m_v > 0$; $A < 1/2$, and the width of the absorbance peak is proportional to $|m_c - m_v|$ (middle right panel). Absorption edge, $m_c \neq m_v$, $m_c > 0$, $m_v < 0$, yielding a step-like feature in absorbance (bottom right panel).

optical spectrum, to identify and quantify the materials with strongest response. Among them, most synthesized and predicted 2D materials for optical applications are semiconductors, whereas intrinsic graphene is a semimetal. Recently, 2D polymorphs of boron (borophene) have attracted great interest[18,19] after reports of successful synthesis.[20,21] They are intrinsically metallic with much higher numbers of free carriers than doped graphene or semiconductors. Although there is rich polymorphism in this material,[22] here we restrict ourselves to the triangular polymorph with $p2mm$ symmetry[23] and calculate its in-plane conductivity along (x) and normal to (y) its zigzag buckled direction. We found borophene heterostructures to show broadband reflectance with $R > 99\%$ for >100 layers from the IR to the UV range, which is superior to that of bulk metals such as even silver. Moreover, in 2D semiconductors, band nesting and excitonic effects result in high absorbance, and we screen out the best absorbers having these properties in each region of the optical spectrum. Our findings reveal and quantify basic properties across a 2D material family as well as identify materials holding promise for design of ultracompact optoelectronics in a wide frequency range.

RESULTS AND DISCUSSION

A 2D material can be viewed as a zero-thickness layer between two semi-infinite dielectric media slabs,[24−26] and its TAR can be obtained using the transfer matrix formulation for waves in layered piecewise-constant media applied to a single interface.[25,27−29] In the case of a 2D interface, the transfer matrix connects the amplitudes of the normally incident and reflected waves across the interface and yields the following (for details, see S1, Supporting Information).

$$T = \frac{4n_1 n_2}{|n_1 + n_2 + \sigma_{2D}Z_{vac}|^2} \tag{1a}$$

$$A = \frac{4n_1 Re\{\sigma_{2D}\}Z_{vac}}{|n_1 + n_2 + \sigma_{2D}Z_{vac}|^2} \tag{1b}$$

$$R = \left| \frac{n_2 - n_1 + \sigma_{2D}Z_{vac}}{n_1 + n_2 + \sigma_{2D}Z_{vac}} \right|^2 \tag{1c}$$

Here $n_{1,2}$ are the refractive indexes on either side of the monolayer, $\sigma_{2D} = \sigma_{2D}(\mathbf{q}, \omega)$ is the optical surface conductivity as a function of frequency (ω) and 2D wavevector ($\mathbf{q}$), and $Z_{vac} = 376.73$ $\Omega = 1/\varepsilon_0 c$ is the impedance of vacuum. Since we consider normal incidence condition, the in-plane component of $\mathbf{q}$ is 0; we henceforth restrict our discussion only to this case. The conductivity of a material determines its optical properties and is estimated from the linear dielectric response as

$$\sigma_{2D}(\mathbf{q}=0, \omega) = i\omega\varepsilon_0(1 - \varepsilon_{3D}(\mathbf{q}=0, \omega))L \tag{2}$$

where $\varepsilon_{3D}(\mathbf{q}, \omega)$ is the head of the full dielectric function calculated for the 2D layer separated from its periodic images by vacuum L. We assume the $\mathbf{q} = 0$ limit and drop the symbol in expressions henceforth.

Phenomenological eqs 1a−1c already reveals a few obviously important features. First, the TAR sum is invariant, $T + A + R = 1$, correctly capturing energy conservation. Second, at very high conductivity, $\sigma_{2D}(\omega) \to \infty$, the layer can reflect fully, $R \approx 1$. (The condition for achieving maximum $R = 1$ in 2D materials from eq 1c is different from that in 3D, where $R = 1$ for any negative real values of dielectric constant.) Third, it is straightforward to see that for $n_1 = n_2 = 1$ the maximum of eq 1b is $A_{max} = 0.5$ (at $\sigma' = 2$ and $\sigma'' = 0$, with $\sigma_{2D}Z_{vac} \equiv \sigma' + i\cdot\sigma''$); that is, absorption reaches 50%, while $T = R = 25\%$. Further microscopic insight can be gleaned from simple physical models as follows.

The first one is 2DEG, a 2D electron gas, representing a metal layer in vacuum, ($n_1 = n_2 = 1$ in eqs 1a−1c). Its 2D conductivity based on the Lindhard dielectric function within the random phase approximation (RPA) can be obtained analytically (see S2, Supporting Information) and yields

$$\sigma_{2D}(\omega) = \frac{i\omega}{m} \frac{ne^2}{(\omega + i/\tau)^2} \tag{3}$$

Here, n is the 2D carrier density, m is the effective mass of electron, and τ is the phenomenological scattering time. The contribution to τ is from electron−electron, electron−phonon,
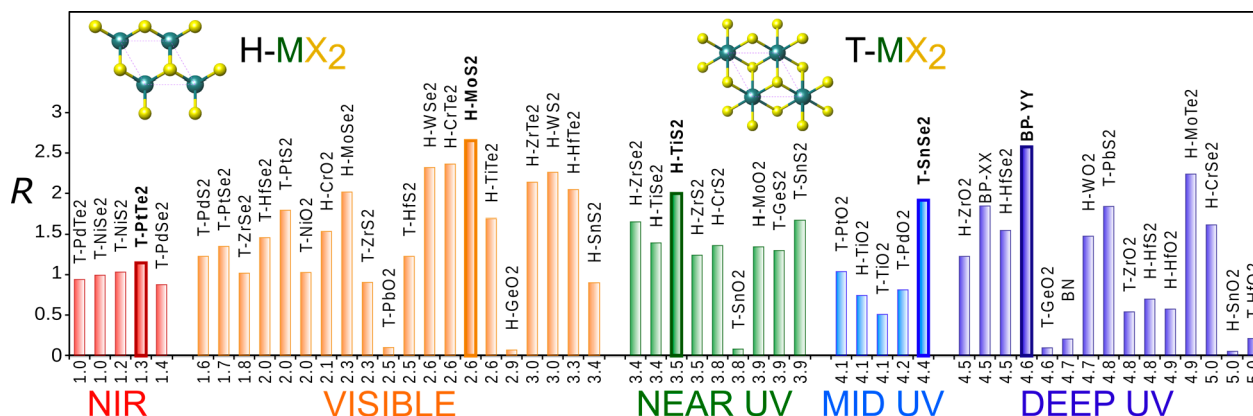
Figure 2. Reflectance, R (%), of 53 monolayers. The best reflective material in each region is highlighted.

and radiative scattering mechanisms. As we consider a pristine, flat, and free-standing 2D material, the scattering due to impurities, defects, and surface roughness is neglected. The TAR values are evaluated by substituting eq 3 into eqs 1a−1c and plotted in Figure 1a for different n, keeping other parameters at their generic values: $m = m_e$ as for free electron and $\tau = 30$ fs. As a single-band metal, 2DEG has very low A, whereas its R increases with n (Figure 1a). It follows from eqs 1c and 3 that for the long waves with THz radiation of $\omega\tau \sim 1$, if the carrier concentration is large in proportion to the relaxation rate, $n \gg \varepsilon_0 e^{-2} mc/\tau$, the 2DEG can be a good reflector with $R \approx 1$. However, in the more common visible range at $\omega\tau \gg 1$, the requirement for strong reflection is rather stringent, $n \gg \varepsilon_0 e^{-2} mc/\omega$ (see S3, Supporting Information); an estimated $n \sim 10^{17}-10^{18}$ cm^{-2} appears unreasonably high for an atomic monolayer but perhaps achievable as a sum over some thickness. Indeed, later we will see that R increases by stacking 2D materials in heterostructure geometry, effectively corresponding to large n.

More instructive in this respect is the second model we examine, a *multiband* case with interband transitions. It can be viewed as electron gas confined by a δz-narrow potential well, in a direction normal to its free x- and y-coordinates; if $\delta z \to 0$, the quantum confinement raises energy spacing so much that only a single band remains. It is reduced to the two-band (in other words, two-level system with dispersion) case when the transition energy is close to the distance between two bands among many. Using Fermi's golden rule, the imaginary part of the dielectric constant $\varepsilon_{2D,imag}$ in a multiband system is given by eq S4.4 (Supporting Information), which is proportional to $|\langle v|p|c\rangle|^2$, the square of the matrix element of momentum, and the joint density of states (JDOS) $\rho_{cv}(\omega) = \sum_k \delta(E_c(k) - E_v(k) - \hbar\omega)$. Introducing phenomenological scattering time τ, we cast ε_{2D} into σ_{2D} in the Lorentz model as

$$\sigma_{2D}(\omega) = \frac{i\omega}{m}\Sigma_j \frac{f_j n e^2}{(\omega^2 - \omega_{0j}^2) + i\omega/\tau}, \quad \Sigma_j f_j = 1 \tag{4}$$

Here, ω_{0j} is the frequency of jth transition and f_j is the oscillator strength. From eq S4.4, $f_j = \frac{2|\langle v|p|c\rangle|^2}{m\hbar\omega_{0j}}$, expressing the conservation of the total number of electrons. The case $\omega_{0j} = 0$ corresponds to intraband transitions and finite frequencies represent interband transitions. We next consider different cases for JDOS depending on the effective masses of the

valence (m_v) and conduction bands (m_c) and use it to calculate TAR under different conditions (for details, see S4, Supporting Information). The left panel of Figure 1b shows the calculated maximum absorbance A_{max} as a function of the difference of the effective masses in the conduction and valence bands, $|m_c - m_v|$.

For *perfect* nesting, $m_c = m_v$. All electrons in the fully occupied band participate in the transition to the empty band at energy $E_0 = E_c - E_v = $ const. The top right panel of Figure 1b shows the absorbance as a function of the photon energy. For perfectly nested bands, $\omega_{0j} = \omega_0 = E_0/\hbar$ and $\sigma_{2D,real} \propto \delta(\omega-\omega_0)$ with $f_j = f_0 = 1$. The width of the absorption peak is determined by the scattering time in the upper and lower bands, due to nonzero imaginary part of electron−phonon and electron−electron self-energy. The δ-function is therefore replaced with a Lorentzian with a width of $1/\tau$, and the maximum absorbance $A_{lim} = 1/2$ is achieved when $c/\tau_{A,max} = ne^2/2\varepsilon_0 m$, where c is the speed of light. In the case of perfect nesting, maximum absorbance can be achieved even when carrier concentration n is low; however, the requirement for the carrier scattering time becomes more stringent as concentration decreases. When the condition for maximum absorbance is satisfied, one has $T = R = 1/4$, and for $\tau > \tau_{A,max}$, $R > T$, whereas for $\tau < \tau_{A,max}$, $T > R$.

For nearly perfect nesting, $m_c \neq m_v$, $\Delta E \gg \hbar/\tau$, where ΔE is the energy window where nesting is significant. In this case, there is a peak in absorption in a narrow range of frequencies around the nesting transition. The absorbance profile for this case is shown in the middle right panel of Figure 1b. Unlike the case of perfect nesting, the width of the peak is determined by ΔE instead of τ. For parabolic bands considered here, $\Delta E = \hbar^2 k_c^2 |m_c - m_v|/2m_c m_v$, where k_c is the cutoff wavevector beyond which band nesting becomes weak. The JDOS in this case is constant and proportional to $m_c m_v/|m_c - m_v|$, and absorbance $A < 1/2$. The maximum absorbance A increases with decreasing $|m_c - m_v|$, approaching the limit of $A_{lim} = 1/2$ when $\Delta E \sim \hbar/\tau$, as seen in the left panel of Figure 1b. This underscores the importance of the existence of a high degree of band nesting in a material to achieve high absorbance.

For absorption edge, $m_c \neq m_v$, $m_c > 0$, $m_v < 0$. Although formally this case is similar to the case of nearly perfect nesting, it is considered separately here in order to emphasize the absence of a sharp absorption peak due to large difference in effective masses. In two dimensions, this corresponds to the JDOS being constant above transition frequency, $\omega_0 = E_0/\hbar$, that is, continuous interband transitions up to $E_0 + \Delta E$, $\Delta E = $
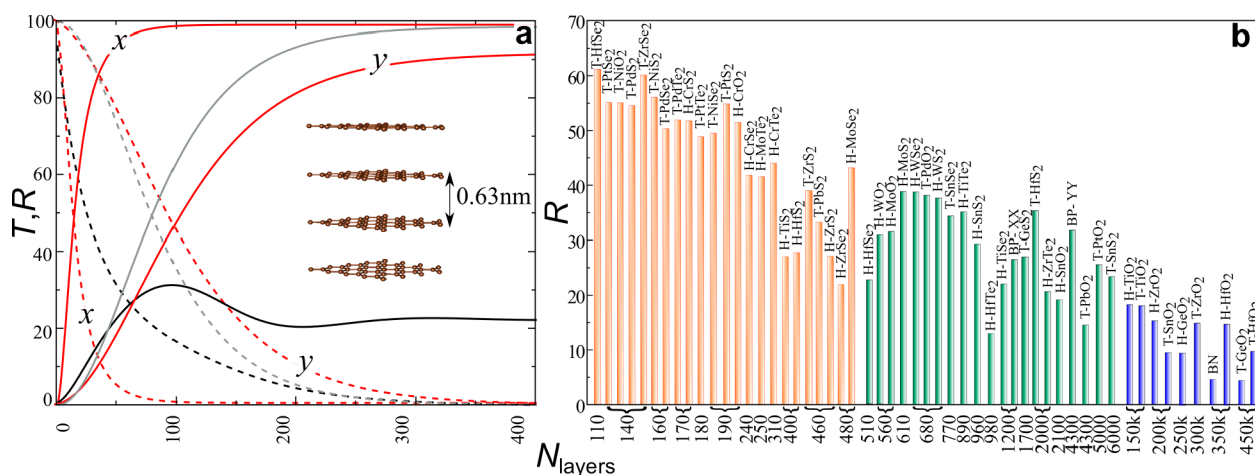
Figure 3. Evolution of (a) T (%) (dashed line) and R (%) (solid line) with number of layers of triangular 2D boron (red) for x and y polarization, doped graphene (E_F = 0.2 eV, black), and bulk silver film (gray) of corresponding thickness using the Lindhard model. T decays exponentially with number of layers. (b) Minimum number of layers required for saturated R (%) (with T = 10^{-3}%) of 53 semiconductor monolayer stacks. All results are at 620 nm (2 eV) of incident light with spacing of 0.63 nm between layers.

$\hbar^2 k_c^2 |m_v - m_v|/2m_c m_v$. Similar to the case of nearly perfect nesting, maximum absorbance A_{max} can approach the value A_{lim} = 1/2 when $|m_c - m_v|$ is small.

Bearing in mind the analytical results for maximum limits on the T, A, and R for 2DEG, we now turn to density functional theory (DFT) calculations for determining the optical properties of 2D materials. We find that DFT yields the Kohn–Sham band gap of ~1.8 eV in MoS_2, which at that level of theory is close to the threshold frequency of absorption, whereas the quasiparticle gap obtained with the G_0W_0 method is ~2.41 eV.[5,30−33] With the inclusion of electron–hole corrections, an excitonic peak appears at ~1.9 eV, reducing the absorption threshold closer to the DFT band gap estimate (see S5 and Figure S5, Supporting Information for details). Thus, although DFT cannot capture excitonic effects, its threshold frequency and the frequency of maximum absorbance are accurately determined within this approximation due to cancellations of various corrections, which is in agreement with previous studies on MoS_2.[5,30−32] We find this trend to be true for other materials, such as H-$MoTe_2$, T-$PtTe_2$, H-TiS_2, and T-$SnSe_2$. Hence, our initial screening of TAR is performed at the DFT level, without G_0W_0+BSE corrections (see S6, Supporting Information for results of unconverged G_0W_0+BSE corrections).

The dielectric function at the DFT level (under RPA) was used to estimate σ_{2D} (eq 2) and TAR (eqs 1a−1c). The calculated TAR for freestanding monolayer graphene and the triangular polymorph of 2D boron is found to be in good agreement with the value in existing literature (Figure S6, Supporting Information).[34,35] Moreover, the estimate of $A(\omega \to 0)$ = 0.023 for graphene is close to the universal analytical constant $(\pi/137)$,[1] showing that the used methodology is accurate. The TAR values are a strong function of ω, as evident from the above examples of graphene and 2D boron, and thus comparison of different 2D materials should be done at specific frequency intervals. Here, we restrict our analysis to energies below 5 eV, as most of the applications involving photodetection do not go beyond the deep-UV range. We now focus on the reflectance of 2D semiconducting monolayers. The maximum of R for $\hbar\omega$ < 5 eV, and corresponding frequencies for the 53 2D semiconductors are plotted in Figure 2. Recently,

a large number of them were experimentally synthesized, and a generalized procedure to make the others was proposed.[36] The materials were assumed to be freestanding, that is, adjacent to vacuum on both sides. The optical properties strongly depend on the relaxation time τ, which is determined by several scattering mechanisms: electron–electron (e–e), electron–phonon (e–ph), impurity, defect, surface roughness scattering, as well as natural line width (n). In our idealized model of pristine flat and free-standing 2D layers, the impurity, defect, and surface scattering mechanisms give null contribution. Hence, the total $1/\tau = 1/\tau_{e-e} + 1/\tau_{e-ph} + 1/\tau_n$ and is dominated by the shortest scattering time. Recent works report that $\tau_{e-e} \sim \tau_{e-ph} \sim$ 13 fs[37,38] in MoS_2 and 22 fs[39] in $MoSe_2$. At the same time, τ_n is at least 100 times longer in these materials,[39,40] and hence, $\tau \sim \tau_{e-e}, \tau_{e-ph}$. In view of the scarcity of values in literature and extensive computational costs for theoretical estimates of τ, we empirically apply the values similar to ones reported for $MoSe_2$ and MoS_2 to all materials. Hence, we choose a reasonable $\tau \sim$ 13 fs for all 53 semiconductors in our work. We find that T-$PtTe_2$, H-MoS_2, H-TiS_2, T-$SnSe_2$, and black phosphorus (BP along y direction; BP-YY) are the most reflecting materials in different optical regimes, as shown in Figure 2. We note that because these materials are semiconductors, their response is solely due to interband transitions resulting in appreciable absorbance that lowers the reflectance.

Although the R of free-standing monolayers is small, it has been shown by Papadakis et al.[41] that heterostructures constructed from stacks of graphene and hexagonal boron nitride (h-BN) show 99.7% reflectance in the mid-IR ranges at a fraction of the weight of noble metals. Based on this approach, we extend our work to study the effect of stacking on the TAR properties of these materials in the visible frequency range (~2 eV) using the transfer matrix method.[26,27] We benchmark our calculations using graphene (doped to $E_F \sim$ 0.2 eV and with relaxation time of ~300 fs) as a reference to compare with previous literature[41] and find our results for R of 250 layers with spacing of 0.67 nm to agree within ±0.5% at λ = 40 μm. Slight discrepancy may arise from the difference in other parameters such as Brillouin zone (BZ) sampling. In the current work, a 600 × 600 × 1 k-point mesh was used. Because
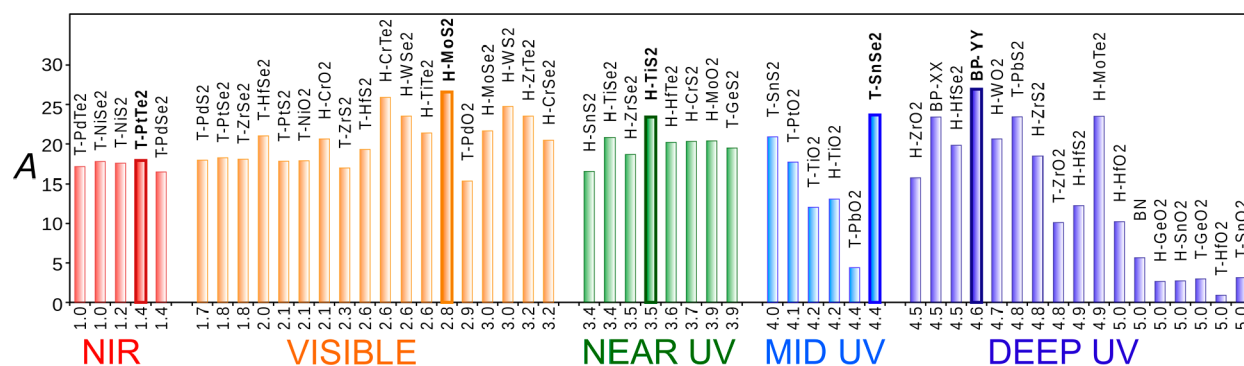
Figure 4. Absorbance, A (%), of 53 monolayers. The best absorbing material in each region is highlighted.

the graphene electronic structure and optical response are symmetric with respect to p- and n-doping at low concentrations, only one type of doping needs to be considered. Here, we consider n-doped graphene.

Unlike graphene, 2D boron is intrinsically metallic with equivalent $n = 5.5 \times 10^{15}$ cm^{-2}, making it an effective single-band metal for frequencies including the visible range. Also, its structural anisotropy is reflected in the anisotropy of the TAR coefficients for different polarizations of light. Due to the high metallicity and anisotropic TAR coefficients, 2D boron exhibits quite high A and R as compared to those of graphene (see S7, Supporting Information for details), hence outperforming it in the visible range. However, the performance of 2D boron with respect to the number of layers has not yet been considered to the best of our knowledge. Moreover, 2D boron exfoliation from a substrate into a free layer has not been achieved yet. In Figure 3a, we compare how the response of 2D boron and doped graphene ($E_F = 0.2$ eV) changes with number of layers at the visible wavelength, $\lambda \sim 620$ nm ($\hbar\omega = 2$ eV), at interlayer separation of 0.63 nm. Our choice of spacing is such that the interlayer interaction is weak, and layers can be treated as independent when applying the transfer matrix method. The calculations for 2D boron were carried out on a $300 \times 300 \times 1$ k-point mesh with a relaxation time of $\sim$29 fs characteristic of bulk metals.[42] We find that R in 2D boron for x polarized light reaches $\sim$98.9% for >100 layers, whereas R of doped graphene saturates at $\sim$21.8% for >200 layers. For y polarization, reflectance of 2D boron is not as high, reaching $\sim$90% for >300 layers. More importantly, the A in multilayer 2D boron is $\sim$0%, as compared with $A \sim 78.1\%$ in multilayer doped graphene. This high reflectance and low absorption in 2D boron is due to the absence of interband transitions up to 3.4 eV, whereas in graphene, the onset of interband transitions is at $2E_F = 0.4$ eV, making highly metallic 2D boron far superior to doped graphene as a reflector in the visible range. Also, graphene needs external (chemical or gate) doping to make it metallic, which could potentially introduce losses or change its electronic structure, whereas 2D boron is intrinsically metallic, thus making it a more attractive reflector material. The advantage of the high threshold for the onset of interband transitions is also clear when comparing R of boron with films of bulk transition metals. In Figure 3a, we show R and T of a silver thin film represented by the Lindhard model with plasma frequency of 3.8 eV and relaxation time of 31 fs.[42] The 2D boron heterostructure has better reflectance than a metal film of the same thickness. Moreover, this heterostructure also shows broadband reflectance from the IR to the UV range (Figure S7, Supporting Information), ideal for designing

ultrathin reflectors in different optical regions. These heterostructures could possibly be used for designing coating materials for protection from high intensity lasers. The 2D boron as well as graphene and hexagonal boron nitride heterostructures[41] outperform metal thin films at long wavelengths, suggesting a potential advantage of 2D heterostructures over bulk materials.

We extend the analysis to the other 53 semiconductors and estimate the minimum number of layers required for R to reach constant value (with zero transmission) at $\lambda \sim 620$ nm, as shown in Figure 3b. Similar to the case of 2D boron heterostructures, the distance between the interlayer chalcogens in semiconductor layers was chosen as 0.63 nm (approximately twice the normal equilibrium van der Waals distance) so that the layers are decoupled and the transfer matrix description can be applied. Hereafter, this value of interlayer distance is used for all heterostructures. This larger interlayer separation can be practically achieved by inserting inert materials such as 2D BN between the layers. To a lesser degree, the interlayer coupling may be decreased by mutually rotating the layers to incoherent turbostratic stacking. It is important to note that, when thickness of the material increases, the phase difference of transmitting light between the layers (which is dependent on λ) increases, and the interference effects from multiple reflections across layers become significant, leading to oscillations in the TAR, as, for example, seen as a peak in R for graphene in Figure 3a. Here, we report the number of layers needed to reach saturation in R (with $T = 10^{-3}\%$). The general trend in Figure 3b shows that materials that reach saturation faster yield higher R values, with a maximum $R \sim 62\%$ for T-HfSe$_2$ at 110 layers. Reflectance for T-PtTe$_2$, H-MoS$_2$, H-TiS$_2$, T-SnSe$_2$, and BP along the y direction saturates at $\sim$48% (180 layers), 39% (610 layers), 27% (400 layers), 34% (770 layers), and 33% (4300 layers), respectively. Other materials, which show saturation at a few thousand layers, are clearly better absorbers/transmitters than reflectors as thin films. Our analysis shows that metals, especially 2D boron, are good reflectors even at visible frequencies, as opposed to semiconductors and doped graphene, which are better absorbers at these wavelengths. These structures open up possibilities for more complex optical metamaterials from 2D layers, as their characteristic dimension a satisfies the condition $\lambda/a \sim 100$ for the metamaterials,[27] yielding $a \sim 5$ nm at a typical optical wavelength $\lambda \sim 500$ nm.

Although 2D semiconductors are not expected to show good reflectance under ambient conditions, they have been found to possess good absorbance. We next study the absorbance of
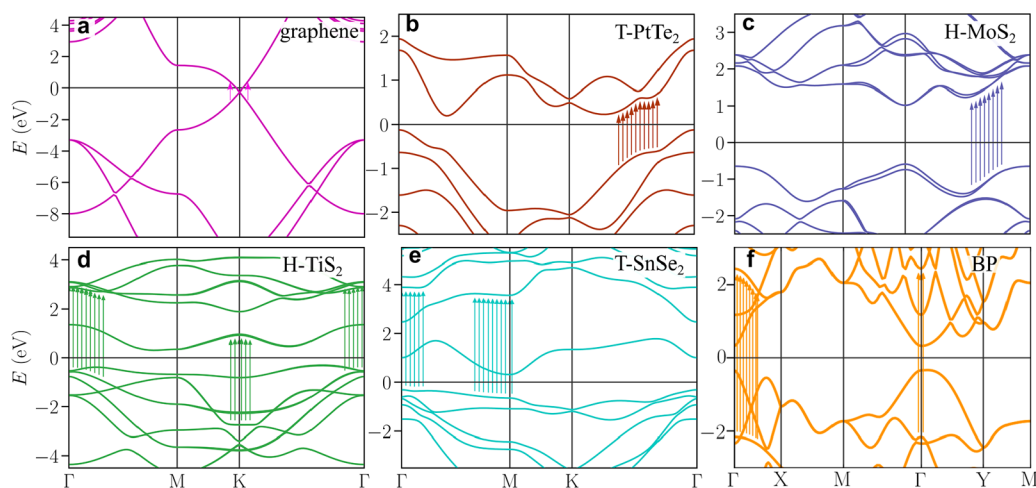
Figure 5. Band structures of (a) n-doped graphene, (b) T-PtTe$_2$, (c) H-MoS$_2$, (d) H-TiS$_2$, (e) T-SnSe$_2$, and (f) BP along the y direction. Vertical arrows show band nesting regions responsible for high absorbance.

monolayers of 53 2D semiconductors. The maximum of A for $\hbar\omega < 5$ eV, and their corresponding frequencies for all materials are plotted in Figure 4. The maximum response is solely due to interband transitions. We screen for materials with best absorbance in each frequency region and find that the best performing materials are T-PtTe$_2$, H-MoS$_2$, H-TiS$_2$, T-SnSe$_2$, and BP along the y direction, in different regions of the electromagnetic spectrum, and BP-YY is the highest absorbing material with $A \sim 27\%$, as shown in Figure 4. Ranking materials according to maximum R and A in a narrow frequency range may not be suitable for all applications. A large (if not maximum) R and A in a broader frequency range may be preferable in some cases, wherein the integral of R and A with respect to frequency is maximized. For this purpose, different 2D materials with maximum R and A in different optical regimes can be vertically stacked into heterostructures to achieve broadband response, thus further expanding the scope of 2D materials in optical nanodevices, as discussed below.

To get further insights into the origins of the large optical response of the semiconducting monolayers in the different regions of the electromagnetic spectrum, we performed noncollinear band structure calculations of the selected 2D materials. The band structures of the materials with largest response are shown in Figure 5. They include metallic n-doped graphene, three indirect-gap semiconductors (T-PtTe$_2$, H-TiS$_2$, and T-SnSe$_2$), and two direct-gap semiconductors (H-MoS$_2$ and black phosphorus). The bands in H-type structures show small spin−orbit splitting, whereas splitting in T-type structures, black phosphorus, and graphene is absent due to their spatial inversion symmetry. Vertical arrows show band nesting regions responsible for the absorption peaks at energies in each of the ranges indicated in Figure 4. Note that in all semiconductors, the transitions responsible for strongest absorption do not occur between band edges. This is expected because bands have opposite curvatures at the edges, precluding the existence of large sections of parallel bands; hence, start of absorption corresponds to the case of an absorption edge (Figure 1b). Such constraints are absent in general, and in comparison to analytical results for 2DEG discussed in the previous section, nesting scenarios correspond to the case of nearly perfect nesting.

In T-PtTe$_2$ and H-MoS$_2$, band nesting occurs between the valence band (VB) and conduction band (CB) at same regions of the BZ, namely, along the ΓK line. The marked transitions in MoS$_2$ correspond to its well-known C excitonic peak, with the energy of ∼2.7 eV. We note that the absorbance in a single MoS$_2$ layer at the C peak (∼26%, about half of the maximum possible value) is much larger than that at the A peak (∼10%), consistent with better nesting conditions away from the band edges. The absorption peak of BP for polarization along the y direction at 4.6 eV originates from transitions at the BZ center (see Figure 5f). Unlike H-MoS$_2$, T-PtTe$_2$ is an indirect-gap semiconductor; however, in T-PtTe$_2$, there are similar transitions at band nesting, yielding the absorbance of ∼17% at 1.4 eV. Note that H-TiS$_2$ and T-SnSe$_2$ have nearly dispersionless bands both below and above the Fermi level which are responsible for their high absorbances at 3.5 and 4.4 eV, respectively.

DFT can provide good qualitative insights into the essential features of the electronic structure, but to have quantitative predictions, one needs to go beyond the one-particle picture of DFT. We next utilize quantitative treatments in the form of post-DFT many-body GW and BSE approaches. We performed calculations of the five 2D semiconductors at the G_0W_0+BSE level, introducing self-energy corrections and capturing excitonic effects and ensuing optical properties. Table 1 shows the DFT-PBE and GW quasiparticle band gaps, and the BSE absorption spectra are shown in Figure 6a−e. As expected, GW corrections to DFT gaps are significant in all cases, ranging from 0.3 to 1 eV. We estimated the dielectric function ($\varepsilon_{3D}(\omega)$) of monolayers in a supercell geometry with vacuum on both sides at the G_0W_0+BSE level. We then

Table 1. GW and DFT-PBE Band Gaps (E_g) of 2D Semiconductors with Strong Optical Response

material	E_g (eV)	
	DFT-PBE	GW
T-PtTe$_2$	0.40	0.69
BP	0.90	1.80
H-TiS$_2$	0.71	1.66
T-SnSe$_2$	0.79	1.78
H-MoS$_2$	1.62	2.41
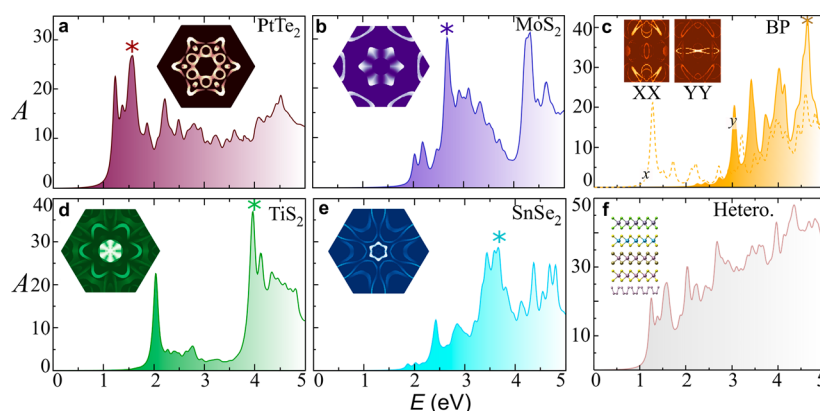
Figure 6. (a–e) BSE absorption spectra (%), with the inset showing band nesting regions in a full Brillouin zone responsible for peaks denoted by ∗. (f) Absorption spectrum (%) of the heterostructure obtained by stacking all five materials in a–e.

converted it to the in-plane conductivity (eq 2) and used eqs 1a–1c to estimate the *TAR*. A τ of ~13 fs, the same as in previous DFT calculations, was used. We find that including excitonic effects indeed changes optical spectra substantially, in particular, by introducing pronounced excitonic peaks and shifting peak positions, as compared to the one-particle DFT spectra. The BSE absorbance spectrum of T-PtTe$_2$ is shown in Figure 6a. We first note the absorbance peak at 1.5 eV, yielding the absorbance of 27% in a single monolayer, which is highest among all considered 2D transition metal dichalcogenides (TMDs) in the near-IR range. In the case of H-MoS$_2$, the band nesting transitions yield an absorbance maximum at 2.7 eV, and the corresponding excitonic C peak is at ~2.66 eV, as seen in Figure 6b. Our BSE results for MoS$_2$ are in quantitative agreement with previous theoretical results and experiment;[5,30−33] in particular, the absorbance of ~30% at the C peak in H-MoS$_2$ compares favorably with the experimental value of ~25%[5,31] (a slight difference is due to the difference in τ between our calculations and experiments). In the absorption spectrum of BP-YY, shown in Figure 6c, we find record predicted absorbance of ~43% at 4.6 eV. Overall, the absorption spectra in Figure 6a–e identify several promising 2D semiconductors with optical properties similar or better than those of the well-known H-MoS$_2$. We also find that combining the materials in a vertical heterostructure improves the overall optical response.[43−45] The five materials (Figure 6a–e) with strongest response were stacked in a heterostructure, and the absorbance was calculated using the transfer matrix method. The heterostructure shows larger *A* (Figure 6f) over a broadband spectrum, when compared with individual materials.

Inclusion of excitonic effects also modulates the reflectance of 2D materials. *R* increases at excitonic resonance in 2D materials, as shown in Figure S3 (Supporting Information). Excitonic resonances in the case of MoS$_2$ are denoted by A, B, and C peaks, which occur at ~1.9, ~2.1 and ~2.66 eV, respectively, as shown in Figure 6b. This resonance between excitonic ground state and its first excited state is similar to the case of perfect nesting (Figure 1b) in our two-band model. The *R* and *A* in such a case depend only on the relaxation time τ, and larger τ gives higher *R* and *A*. The increase in *R* and *A* of 2D MoS$_2$ at excitonic resonance is also seen in our BSE calculations at different τ values (Figure S9, Supporting Information). Therefore, cleaner samples at low temperatures will have smaller scattering rates (larger τ) and hence exhibit

improved *R* and *A*. Recently, a *R* of >80% was experimentally observed in 2D MoSe$_2$ at excitonic resonance due to larger τ at low temperatures, signifying that sample quality and temperature play a significant role in improving the optical response.[40] In addition to cleanliness, the flatness of samples also affects the sharpness of the *TAR* peaks.[46] Depending upon the substrate flatness, the 2D material can experience local distortions, leading to loss of structural symmetry, causing additional scattering and inhomogeneous broadening. Our calculations are for strictly flat, free-standing, pristine materials, and hence, inhomogeneous broadening is not included in our model. Here, we use relaxation time approximation, where all the other scattering mechanisms (electron−electron, electron−phonon, and radiative) are combined into a single homogeneous broadening term. In experiments, the flatness can be assured by using atomically smooth noninteracting substrates such as h-BN.[46]

Another important characteristic of optical materials is skin/penetration depth, which measures how deep the incident electromagnetic radiation penetrates the material. As the TMD monolayers exhibit promising absorbance values (smaller skin depth), we extend our transfer matrix formalism to the G_0W_0+BSE analysis to estimate the skin depth of the select TMD monolayers at peak frequencies marked in Figure 6a−e. In Table 2, we report the distance at which the transmittance *T* falls to $1/e^2$ of its value at the surface.

Our estimate of skin depth of H-MoS$_2$ is in good agreement with experimental observations of ~5 nm at ~3 eV,[47] with discrepancy arising from the quality of samples (*i.e.*, different scattering times) and difference in interlayer distance. Hence, our estimates can be used to gain a quantitative as well as qualitative measure of comparison among the compounds. We

Table 2. Skin Depth of TMD Stacked Monolayers at Frequencies Corresponding to Peaks in Absorbance in Figure 6a−e (Skin Depth of Bulk Silver Is Given for Comparison)

material	peak frequency (eV)	skin depth (nm)	
		material	bulk Ag
T-PtTe$_2$	1.58	4.96	18
H-MoS$_2$	2.66	3.0	22
BP	4.6	1.1	25
H-TiS$_2$	3.95	1.96	25
T-SnSe$_2$	3.68	3.2	25

find that BP exhibits the smallest skin depth of ~1 nm (4.6 eV), in agreement with its highest predicted absorbance of ~43%. In comparison, it is seen from Table 2 that the skin depth of bulk Ag is approximately 5−10 times larger than that of TMDs and that of stacked 2D boron reaches 19 nm at 2 eV, reaffirming the exceptional absorption capacity of 2D TMDs and BP, with possible applications for radiation shielding.

CONCLUSIONS

In conclusion, we carried out a computational survey of the optoelectronic properties of 2D materials, in particular, their transmittance, absorbance, and reflectance (TAR), with the goal of identifying materials with strongest optical response in different frequency ranges. Analytically, we gain microscopic insights into the origins of maximum response. Using a single-band model, we find that 2D metals have high reflectance in the THz regime; however, for maximum broadband R, high carrier concentration is required. Our results show that vertical heterostructures formed from stacking of 2D boron have broadband reflectance from the IR to the UV range and outperform doped graphene and bulk silver, with reflectance reaching ~99% for >100 layers. Phenomenologically, free-standing 2D materials have absolute absorbance limit of $A_{lim} = 1/2$. The analytical two-band model elucidates the role of band nesting to attain A_{lim}. We find from G_0W_0+BSE calculations that among all 2D semiconductors considered, T-PtTe$_2$, H-MoS$_2$, H-TiS$_2$, T-SnSe$_2$, and black phosphorus have absorbances $\gtrsim$30% in the near-IR, visible, near-UV, mid-UV, and deep-UV regions, respectively, mediated by band nesting and excitonic effects. Low scattering rates are important for achieving A_{lim} in these materials. Stacking these materials in a vertical heterostructure further improves the overall optical response. A larger A approaching the A_{lim} value over a broadband spectrum is achieved in the van der Waals heterostructures. The higher absorbance of BP and TMD monolayers is also manifested in their skin depth, which is at least 5−10 times smaller than bulk silver. These materials with maximum response in different optical regimes are ideal for compact optoelectronics and understanding light−matter interactions.

METHODS

We carried out first-principles density functional theory calculations with dielectric response as implemented in the VASP[48] and GPAW[49] codes. The linear dielectric response was estimated for both the noninteracting Kohn−Sham system under random phase approximation, as well as with self-energy corrections to Kohn−Sham single-particle eigenvalues and accounting for electron−hole interactions using G_0W_0+BSE formalism. The initial screening of optical properties (under RPA with PBE functional) of two-dimensional materials was done by extracting the dielectric function $\varepsilon(\omega)$ for structures listed in the van der Waals heterostructure database in the Computational Materials Repository.[50,51] Note that the database comprises of structural information of 2D nonmagnetic semiconducting transition metal dichalcogenides and oxides with theoretical negative heats of formation and is also referenced in the Inorganic Crystal Structure Database.[52] Recently, a large number of them were experimentally synthesized, and a generalized procedure to make the others was proposed.[36]

The dielectric response beyond RPA was calculated using the single-shot G_0W_0 procedure together with solution of the Bethe−Salpeter equation implemented in VASP. This technique correctly accounts for electron−hole interaction necessary to obtain an accurate excitonic spectra. A vacuum of 18 Å was used along the out-of-plane direction to reduce the interaction between the periodic images.

Spin−orbit coupling was included in all the calculations. A Γ-centered grid of $24 \times 24 \times 1$ was used to sample the Brillouin zone. The wave functions were expanded in a plane wave basis with an energy cutoff of 500 eV. The Kohn−Sham orbitals obtained using the PBE functional were used as a starting guess for G_0W_0 calculation. A plane wave cutoff of 333 eV and a frequency grid of 225 points were used for calculating the response function in the G_0W_0 approach. A total of $6N$ bands, where N is the total number of valence electrons in the material, was used in the dielectric function and G_0W_0 calculation. BSE calculations were performed using 50 bands (20 in valence and 30 in conduction band). These parameters were optimized to obtain a converged optical spectrum (see S12, Supporting Information for convergence results). We note that, the converged G_0W_0+BSE analysis was carried out for 5 selected materials (see main text). A calculation for the remaining materials should also yield more realistic estimates.

ASSOCIATED CONTENT

ⓢ Supporting Information

The Supporting Information is available free of charge on the ACS Publications website at DOI: 10.1021/acsnano.8b03754.

Transmittance, absorbance, and reflectance (TAR) of a 2D material using transfer matrix method, Lindhard dielectric function for a 2D electron gas, maximum reflectance condition, JDOS and maximum absorbance condition, RPA vs BSE dielectric information, R and A of 53 monolayers calculated with unconverged G_0W_0+BSE, comparison of TAR for monolayers of graphene and boron, comparison of the reflectance of heterostructures of 2D boron and doped graphene, dielectric response in the 2D limit, transmittance of 53 monolayers in the UV range, R and A of MoS$_2$ at different values of τ, convergence results, and validation of transfer matrix method (PDF)

AUTHOR INFORMATION

Corresponding Author

*E-mail: biy@rice.edu.

ORCID ⓘ

Sharmila N. Shirodkar: 0000-0002-9040-5858
Alex Kutana: 0000-0001-6405-6466

Notes

The authors declare no competing financial interest.

REFERENCES

(1) Nair, R. R.; Blake, P.; Grigorenko, A. N.; Novoselov, K. S.; Booth, T. J.; Stauber, T.; Peres, N. M. R.; Geim, A. K. Fine Structure Constant Defines Visual Transparency of Graphene. *Science* **2008**, *320*, 1308−1308.
(2) Gutiérrez, H. R.; Perea-López, N.; Elías, A. L.; Berkdemir, A.; Wang, B.; Lv, R.; López-Urías, F.; Crespi, V. H.; Terrones, H.; Terrones, M. Extraordinary Room-Temperature Photoluminescence in Triangular WS2Monolayers. *Nano Lett.* **2013**, *13*, 3447−3454.

(3) Xia, F.; Wang, H.; Xiao, D.; Dubey, M.; Ramasubramaniam, A. Two-Dimensional Material Nanophotonics. *Nat. Photonics* **2014**, *8*, 899−907.

(4) Mak, K. F.; Shan, J. Photonics and Optoelectronics of 2D Semiconductor Transition Metal Dichalcogenides. *Nat. Photonics* **2016**, *10*, 216−226.

(5) Mak, K. F.; Lee, C.; Hone, J.; Shan, J.; Heinz, T. F. Atomically Thin MoS2: A New Direct-Gap Semiconductor. *Phys. Rev. Lett.* **2010**, *105*, 136805.

(6) Splendiani, A.; Sun, L.; Zhang, Y.; Li, T.; Kim, J.; Chim, C.-Y.; Galli, G.; Wang, F. Emerging Photoluminescence in Monolayer MoS2. *Nano Lett.* **2010**, *10*, 1271−1275.

(7) Eda, G.; Yamaguchi, H.; Voiry, D.; Fujita, T.; Chen, M.; Chhowalla, M. Photoluminescence from Chemically Exfoliated MoS2. *Nano Lett.* **2011**, *11*, 5111−5116.

(8) Yu, P.; Cardona, M. *Fundamentals of Semiconductors: Physics and Materials Properties*; Springer Science & Business Media, 2010.

(9) Yoffe, A. D. Low-Dimensional Systems: Quantum Size Effects and Electronic Properties of Semiconductor Microcrystallites (Zero-Dimensional Systems) and Some Quasi-Two-Dimensional Systems. *Adv. Phys.* **1993**, *42*, 173−262.

(10) Sun, Z.; Martinez, A.; Wang, F. Optical Modulators with 2D Layered Materials. *Nat. Photonics* **2016**, *10*, 227−238.

(11) Jariwala, D.; Sangwan, V. K.; Lauhon, L. J.; Marks, T. J.; Hersam, M. C. Emerging Device Applications for Semiconducting Two-Dimensional Transition Metal Dichalcogenides. *ACS Nano* **2014**, *8*, 1102−1120.

(12) Fiori, G.; Bonaccorso, F.; Iannaccone, G.; Palacios, T.; Neumaier, D.; Seabaugh, A.; Banerjee, S. K.; Colombo, L. Electronics Based on Two-Dimensional Materials. *Nat. Nanotechnol.* **2014**, *9*, 768−779.

(13) Tsai, M.-L.; Su, S.-H.; Chang, J.-K.; Tsai, D.-S.; Chen, C.-H.; Wu, C.-I.; Li, L.-J.; Chen, L.-J.; He, J.-H. Monolayer MoS2 Heterojunction Solar Cells. *ACS Nano* **2014**, *8*, 8317−8322.

(14) Ferrari, A. C.; Bonaccorso, F.; Fal'ko, V.; Novoselov, K. S.; Roche, S.; Bøggild, P.; Borini, S.; Koppens, F. H. L.; Palermo, V.; Pugno, N.; Sordan, R.; Bianco, A.; Ballerini, L.; Prato, M.; Lidorikis, E.; Kivioja, J.; Marinelli, C.; Ryhänen, T.; Morpurgo, A.; Garrido, J. A.; et al. Science and Technology Roadmap for Graphene, Related Two-Dimensional Crystals, and Hybrid Systems. *Nanoscale* **2015**, *7*, 4598−4810.

(15) Yin, Z.; Li, H.; Li, H.; Jiang, L.; Shi, Y.; Sun, Y.; Lu, G.; Zhang, Q.; Chen, X.; Zhang, H. Single-Layer MoS2 Phototransistors. *ACS Nano* **2012**, *6*, 74−80.

(16) Bonaccorso, F.; Colombo, L.; Yu, G.; Stoller, M.; Tozzini, V.; Ferrari, A. C.; Ruoff, R. S.; Pellegrini, V. Graphene, Related Two-Dimensional Crystals, and Hybrid Systems for Energy Conversion and Storage. *Science* **2015**, *347*, 1246501.

(17) Liu, X.; Galfsky, T.; Sun, Z.; Xia, F.; Lin, E.; Lee, Y.-H.; Kéna-Cohen, S.; Menon, V. M. Strong Light−Matter Coupling in Two-Dimensional Atomic Crystals. *Nat. Photonics* **2015**, *9*, 30−34.

(18) Zhang, Z.; Penev, E. S.; Yakobson, B. I. Two-Dimensional Materials: Polyphony in B Flat. *Nat. Chem.* **2016**, *8*, 525−527.

(19) Zhang, Z.; Penev, E. S.; Yakobson, B. I. Two-Dimensional Boron: Structures, Properties and Applications. *Chem. Soc. Rev.* **2017**, *46*, 6746−6763.

(20) Mannix, A. J.; Zhou, X.-F.; Kiraly, B.; Wood, J. D.; Alducin, D.; Myers, B. D.; Liu, X.; Fisher, B. L.; Santiago, U.; Guest, J. R.; Yacaman, M. J.; Ponce, A.; Oganov, A. R.; Hersam, M. C.; Guisinger, N. P. Synthesis of Borophenes: Anisotropic, Two-Dimensional Boron Polymorphs. *Science* **2015**, *350*, 1513−1516.

(21) Feng, B.; Zhang, J.; Zhong, Q.; Li, W.; Li, S.; Li, H.; Cheng, P.; Meng, S.; Chen, L.; Wu, K. Experimental Realization of Two-Dimensional Boron Sheets. *Nat. Chem.* **2016**, *8*, 563−568.

(22) Penev, E. S.; Bhowmick, S.; Sadrzadeh, A.; Yakobson, B. I. Polymorphism of Two-Dimensional Boron. *Nano Lett.* **2012**, *12*, 2441−2445.

(23) Penev, E. S.; Kutana, A.; Yakobson, B. I. Can. Two-Dimensional Boron Superconduct? *Nano Lett.* **2016**, *16*, 2522−2526.

(24) Sensale-Rodriguez, B.; Yan, R.; Kelly, M. M.; Fang, T.; Tahy, K.; Hwang, W. S.; Jena, D.; Liu, L.; Xing, H. G. Broadband Graphene Terahertz Modulators Enabled by Intraband Transitions. *Nat. Commun.* **2012**, *3*, 780.

(25) Saleh, B. E. A.; Teich, M. C. *Fundamentals of Photonics*, 2nd ed.; Wiley Series in Pure and Applied Optics, 2007.

(26) Zhan, T.; Shi, X.; Dai, Y.; Liu, X.; Zi, J. Transfer Matrix Method for Optics in Graphene Layers. *J. Phys.: Condens. Matter* **2013**, *25*, 215301.

(27) Pendry, J. B. Calculating Photonic Band Structure. *J. Phys.: Condens. Matter* **1996**, *8*, 1085.

(28) Katsidis, C. C.; Siapkas, D. I. General Transfer-Matrix Method for Optical Multilayer Systems with Coherent, Partially Coherent, and Incoherent Interference. *Appl. Opt.* **2002**, *41*, 3978−3987.

(29) Li, Y.; Heinz, T. F. Two-Dimensional Models for the Optical Response of Thin Films. *2D Mater.* **2018**, *5*, 025021.

(30) Qiu, D. Y.; da Jornada, F. H.; Louie, S. G. Optical Spectrum of MoS2: Many-Body Effects and Diversity of Exciton States. *Phys. Rev. Lett.* **2013**, *111*, 216805.

(31) Li, Y.; Chernikov, A.; Zhang, X.; Rigosi, A.; Hill, H. M.; van der Zande, A. M.; Chenet, D. A.; Shih, E.-M.; Hone, J.; Heinz, T. F. Measurement of the Optical Dielectric Function of Monolayer Transition-Metal Dichalcogenides: MoS2, MoSe2, WS2, and WSe2. *Phys. Rev. B: Condens. Matter Mater. Phys.* **2014**, *90*, 205422.

(32) Okada, M.; Kutana, A.; Kureishi, Y.; Kobayashi, Y.; Saito, Y.; Saito, T.; Watanabe, K.; Taniguchi, T.; Gupta, S.; Miyata, Y.; Yakobson, B. I.; Shinohara, H.; Kitaura, R. Direct and Indirect Interlayer Excitons in a van Der Waals Heterostructure of HBN/WS2/MoS2/HBN. *ACS Nano* **2018**, *12*, 2498−2505.

(33) Gupta, S.; Shirodkar, S. N.; Kaplan, D.; Swaminathan, V.; Yakobson, B. I. Franck Condon Shift Assessment in 2D MoS 2. *J. Phys.: Condens. Matter* **2018**, *30*, 095501.

(34) Matthes, L.; Pulci, O.; Bechstedt, F. Optical Properties of Two-Dimensional Honeycomb Crystals Graphene, Silicene, Germanene, and Tinene from First Principles. *New J. Phys.* **2014**, *16*, 105007.

(35) Lherbier, A.; Botello-Méndez, A. R.; Charlier, J.-C. Electronic and Optical Properties of Pristine and Oxidized Borophene. *2D Mater.* **2016**, *3*, 045006.

(36) Zhou, J.; Lin, J.; Huang, X.; Zhou, Y.; Chen, Y.; Xia, J.; Wang, H.; Xie, Y.; Yu, H.; Lei, J.; Wu, D.; Liu, F.; Fu, Q.; Zeng, Q.; Hsu, C.; Yang, C.; Lu, L.; Yu, T.; Shen, Z.; Lin, H.; et al. A Library of Atomically Thin Metal Chalcogenides. *Nature* **2018**, *556*, 355−359.

(37) Molina-Sánchez, A.; Palummo, M.; Marini, A.; Wirtz, L. Temperature-Dependent Excitonic Effects in the Optical Properties of Single-Layer MoS2. *Phys. Rev. B: Condens. Matter Mater. Phys.* **2016**, *93*, 155435.

(38) Cadiz, F.; Courtade, E.; Robert, C.; Wang, G.; Shen, Y.; Cai, H.; Taniguchi, T.; Watanabe, K.; Carrere, H.; Lagarde, D.; Manca, M.; Amand, T.; Renucci, P.; Tongay, S.; Marie, X.; Urbaszek, B. Excitonic Linewidth Approaching the Homogeneous Limit in MoS2-Based van Der Waals Heterostructures. *Phys. Rev. X* **2017**, *7*, 021026.

(39) Scuri, G.; Zhou, Y.; High, A. A.; Wild, D. S.; Shu, C.; De Greve, K.; Jauregui, L. A.; Taniguchi, T.; Watanabe, K.; Kim, P.; Lukin, M. D.; Park, H. Large Excitonic Reflectivity of Monolayer MoSe 2 Encapsulated in Hexagonal Boron Nitride. *Phys. Rev. Lett.* **2018**, *120*, 037402.

(40) Robert, C.; Lagarde, D.; Cadiz, F.; Wang, G.; Lassagne, B.; Amand, T.; Balocchi, A.; Renucci, P.; Tongay, S.; Urbaszek, B.; Marie, X. Exciton Radiative Lifetime in Transition Metal Dichalcogenide Monolayers. *Phys. Rev. B: Condens. Matter Mater. Phys.* **2016**, *93*, 205423.

(41) Papadakis, G. T.; Narang, P.; Sundararaman, R.; Rivera, N.; Buljan, H.; Engheta, N.; Soljačić, M. Ultralight Angstrom-Scale Optimal Optical Reflectors. *ACS Photonics* **2018**, *5*, 384−389.

(42) Johnson, P. B.; Christy, R. W. Optical Constants of the Noble Metals. *Phys. Rev. B* **1972**, *6*, 4370−4379.

(43) Britnell, L.; Ribeiro, R. M.; Eckmann, A.; Jalil, R.; Belle, B. D.; Mishchenko, A.; Kim, Y.-J.; Gorbachev, R. V.; Georgiou, T.; Morozov, S. V.; Grigorenko, A. N.; Geim, A. K.; Casiraghi, C.; Neto, A. H. C.;

Novoselov, K. S. Strong Light-Matter Interactions in Heterostructures of Atomically Thin Films. *Science* **2013**, *340*, 1311−1314.

(44) Novoselov, K. S.; Mishchenko, A.; Carvalho, A.; Castro Neto, A. H. 2D Materials and van Der Waals Heterostructures. *Science* **2016**, *353*, aac9439.

(45) Liu, Y.; Shivananju, B. N.; Wang, Y.; Zhang, Y.; Yu, W.; Xiao, S.; Sun, T.; Ma, W.; Mu, H.; Lin, S.; Zhang, H.; Lu, Y.; Qiu, C.; Li, S.; Bao, Q. Highly Efficient and Air-Stable Infrared Photodetector Based on 2D Layered Graphene−Black Phosphorus Heterostructure. *ACS Appl. Mater. Interfaces* **2017**, *9*, 36137−36145.

(46) Okada, M.; Sawazaki, T.; Watanabe, K.; Taniguch, T.; Hibino, H.; Shinohara, H.; Kitaura, R. Direct Chemical Vapor Deposition Growth of WS2 Atomic Layers on Hexagonal Boron Nitride. *ACS Nano* **2014**, *8*, 8273−8277.

(47) Liu, H.-L.; Shen, C.-C.; Su, S.-H.; Hsu, C.-L.; Li, M.-Y.; Li, L.-J. Optical Properties of Monolayer Transition Metal Dichalcogenides Probed by Spectroscopic Ellipsometry. *Appl. Phys. Lett.* **2014**, *105*, 201905.

(48) Gajdoš, M.; Hummer, K.; Kresse, G.; Furthmüller, J.; Bechstedt, F. Linear Optical Properties in the Projector-Augmented Wave Methodology. *Phys. Rev. B: Condens. Matter Mater. Phys.* **2006**, *73*, 045112.

(49) Enkovaara, J.; Rostgaard, C.; Mortensen, J. J.; Chen, J.; Dułak, M.; Ferrighi, L.; Gavnholt, J.; Glinsvad, C.; Haikola, V.; Hansen, H. A.; Kristoffersen, H. H.; Kuisma, M.; Larsen, A. H.; Lehtovaara, L.; Ljungberg, M.; Lopez-Acevedo, O.; Moses, P. G.; Ojanen, J.; Olsen, T.; Petzold, V.; et al. Electronic Structure Calculations with GPAW: A Real-Space Implementation of the Projector Augmented-Wave Method. *J. Phys.: Condens. Matter* **2010**, *22*, 253202.

(50) Andersen, K.; Latini, S.; Thygesen, K. S. Dielectric Genome of van Der Waals Heterostructures. *Nano Lett.* **2015**, *15*, 4616−4621.

(51) Rasmussen, F. A.; Thygesen, K. S. Computational 2D Materials Database: Electronic Structure of Transition-Metal Dichalcogenides and Oxides. *J. Phys. Chem. C* **2015**, *119*, 13169−13183.

(52) Lebègue, S.; Björkman, T.; Klintenberg, M.; Nieminen, R. M.; Eriksson, O. Two-Dimensional Materials from Data Filtering and Ab Initio Calculations. *Phys. Rev. X* **2013**, *3*, 031002.